Coordination engineering and electronic structure modulation of FeNi dual-single-atoms encapsulated in N, P-codoped 3D hierarchically porous carbon electrocatalyst for synergistically boosting oxygen reduction reaction

Lu Zhang, Dong-Hui Wu, Mahmood Ul Haq, Jiu-Ju Feng, Fa Yang [*], Ai-Jun Wang [*]

Key laboratory of the Ministry of Education for Advanced Catalysis Materials, College of Chemistry and Materials Science, College of Geography and Environmental Sciences, Zhejiang Normal University, Jinhua 321004, China

A R T I C L E   I N F O

A B S T R A C T

With the increasing energy and environmental issues in recent years, it is vital to explore inexpensive and highly activated oxidation reduction reaction (ORR) catalysts for next generation energy storage and conversion devices such as zinc-air batteries. Herein, FeNi dual-single-atoms were efficiently encapsulated into N,P-codoped 3D hierarchically porous carbon (FeNi DSAs/N,P-PC) by a simple one-step pyrolysis. The resulting FeNi DSAs/N,P-PC catalyst exhibited the better ORR activity with the positive onset potential ($E_{onset} = 1.02$ V) and half-wave potential ($E_{1/2} = 0.88$ V) over commercial Pt/C, and performed well in the assembled zinc-air batteries (peak power density of 124.73 mW cm^{-2}, and long-term charge/discharge stable cycling for 330 h). The XAFS analysis clearly displayed the coordination structure and interactions of the FeNi dual atoms. The DFT calculations show that P-O bonds have great influence on the electronic structure of the FeNi dual atoms. And Ni site can effectively modulate the electronic structure of the Fe site to promote charge transfer and further reduce the energy barrier of the rate-limiting step. This strategy provides a viable strategy for development of low-cost high-performance transition metal diatomic catalysts suitable for energy conversion and storage devices.

1. Introduction

In response to the energy and environmental concerns arising from the long-standing fossil fuel-based energy consumption pattern, it is essential to develop advanced clean and sustainable energy storage systems [1]. Among them, metal-air batteries, particularly zinc-air batteries, have received a large attention due to the high safety, low cost, environmentally friendly sustainability and high theoretical energy density [2]. However, the technical limitations associated with zinc air batteries, in particular the severe lag in the kinetics of the oxygen reduction reaction (ORR) at the air cathode, are considered to be a complicated bottleneck for their practical applications [3]. Although Pt-based catalysts greatly improved the ORR kinetics, the scarcity of their resources and low tolerance to methanol crossover severely prevent the potential applications [4].

In recent years, transition metal (TM)-based catalysts incorporated into carbon substrates show high ORR catalytic activity and cycling stability due to their tunable elemental compositions and electronic structures, which are gradually developed as the most promising substitutes for platinum-based catalysts [5]. Among them, TM single-atom catalysts (SACs) have made an important contribution to improving the ORR catalytic kinetics, owing to their extremely high atomic utilization, tunable coordination environment and small size effect [6,7].

However, individual metal atoms have a high surface free energy and tendency to agglomerate during the synthesis and long-term catalytic reactions courses, which can easily form nanoparticles, thus changing the character of the active sites and adversely affecting the stability [8, 9]. Also, the SACs have a single active center and there is an unbreakable linear relationship between the adsorption energies of the ORR intermediates, which fundamentally limits the catalytic efficiency [10]. It is still a major challenge to overcome these problems for the practical application of SACs to energy conversion and storage technologies.

Metal sites were found to be reaction centers for reactant activation, and their catalytic activity was affected by the electronic structure and

---

* Corresponding authors.
E-mail addresses: yangfa@zjnu.edu.cn (F. Yang), ajwang@zjnu.cn (A.-J. Wang).

coordination environment. Increasing the number of coordination unsaturated metal sites and adjusting the electronic structure can effectively regulate the performance of metal sites [11]. By contrast, dual atomic catalysts (DSAs) effectively surpass the limitations of SACs by introducing a second metal to modulate the electronic state of the original single atom and provide adjacent active sites [12]. Generally, the significant synergy, distance-enhancing and electronic effects between two the heteronuclear metal atoms in adjacent coordination allow for easier regulation of the d-band center, thus facilitating the adsorption/desorption process of the ORR intermediates on the catalyst surface and breaking the linear relationship between the adsorption energies of the reaction intermediates [13,14]. Recently, TM-based diatomic catalysts have been widely explored, where N-doped carbon-loaded TM diatomic sites (TM-N_x-C-DSAs) exhibit attractive ORR activity [15]. However, the high electronegativity of the N atoms from the M-N_4 moiety somewhat hinders the adsorption of the oxygenated intermediates to the metal center, thereby increasing the reaction potential [16].

To date, the introduction of exotic non-metallic atoms (e.g., S, P, B and F) into N-doped carbon-supported DSAs is recognized as effective strategy to further increase the ORR activity [17,18]. Commonly, the introduction of heteroatoms in the carbon matrix can effectively drive the long-range electron leaving domains in the metal center, increase the intrinsic activity of the active site and optimize the adsorption energy of the ORR reaction intermediates, thanks to their different atomic radii and electronegativity [19]. Besides, heteroatoms can form chemical bonds to stabilize the original metal sites, avoid the atomic agglomeration and improve the long-term operational stability of the catalyst [20]. P as a homologue of N, has a strong electron giving ability and a larger covalent radius, whose introduction into the TM-Nx-C-DSAs can effectively break the symmetrical coordination configuration, which is a promising approach to improve the ORR performance [21].

Furthermore, morphological and structural engineering of carbon substrates is important in enhancing the ORR catalytic properties of the DSAs [22]. For the DSAs, the catalytic activity is directly influenced by the density of the active sites that are exposed to electrolyte, and a carbon substrate with a three-dimensional (3D) layered porous structure can provide increased accessibility to the active site that further improve atom utilization [23]. It is an effective way for utilization of micro-/macro- structures of the carbon matrix with large porosity to promote the interfacial mass and charge transport [24].

For the preparation of monoatomic catalysts, defect sites are constructed on the surface of the carrier, and C defects, S defects and metal defects of the carrier are used as "traps" to capture metal precursors. The formed single atom is then stabilized by the charge transfer effect between the metal single atom and the defect site [25]. Herein, we develop a simple strategy for Fe/Ni bi-atomic sites. By creating defects and introducing heteroatom dopants as "traps" to anchor Fe and Ni metal atoms, an N,P co-doped 3D layered porous carbon (FeNi DSA/N,P-PC) catalyst was successfully obtained. The catalytic activity of the resulting catalyst was examined by a series of characterizations such as electron microscopy and synchrotron X-ray absorption fine structure (XAFS), as well as electrochemical methods using the ORR as a baseline model. Furthermore, the DFT calculations were carried out for the FeNi DSAs/N,P-PC system to elucidate the corresponding ORR catalytic mechanism.

2. Experimental

2.1. Synthesis of FeNi DSAs/N,P-PC

Typically, g-C_3N_4 was synthesized based on the earlier literature [26]. In brief, 5 g of melamine was transferred into a tube furnace and heated to 550 °C in air atmosphere with a heating rate of 5 °C min^{-1}, coupled by holding for 2 h. A pale yellow powder was obtained by grinding for later use.

For typical preparation of the FeNi DSAs/N,P-PC, 1.2 g of glucose, 0.8 g of g-C_3N_4, 0.8 g of magnesium carbonate, 0.017 g of $FeCl_3$, 0.0125 g of Ni(OCOCH$_3$)$_2$·4 H$_2$O and 0.066 g of phytic acid were mixed and ground in a mortar for 30 min. Next, the mixture was transferred to a tube furnace, heated to 800°C in a N_2 atmosphere at a heating rate of 5 °C min^{-1} and maintained for 2 h. The product was further immersed into a HCl solution (3.0 M), and stirred for 2 h at 60 °C, followed by standing for 10 h to remove impurities. Finally, the product was washed for several times with water and ethanol, and vacuum-dried at 60 °C.

Control samples were obtained by either modulating the calcination temperature (e.g., 700 °C and 900 °C), while the other experimental conditions were kept the same as before, denoted as FeNi DSAs/N,P-PC-700 and FeNi DSAs/N,P-PC-900, respectively. Similarly, monometallic Fe/N,P-PC and Ni/N,P-PC were synthesized by the same way as that of the FeNi DSAs/N,P-PC, except by employing individual $FeCl_3$ and Ni (OCOCH$_3$)$_2$·4 H$_2$O as the precursor, respectively.

Detailed information about the characterizations and electrochemical measurements and density functional theory simulation were provided in supplementary information.

3. Results and discussion

3.1. Characterizations

Fig. 1 shows the preparation route of the above FeNi DSAs/N,P-PC by grinding a mixture of glucose, g-C_3N_4, alkaline magnesium carbonate, metal salts and phytic acid, accompanied by its pyrolysis at 800 °C in N_2 atmosphere. At the initial stage, glucose chelates the metal ions that can be uniformly dispersed onto g-C_3N_4 to provide additional source of carbon for subsequent pyrolysis. When the temperature rises, the glucose-chelated metal complex is incorporated into the six-fold cavity of g-C_3N_4 to form stable Fe/Ni single-atom site [27]. In this step, the metal species are able to coordinate with the nitrogen doped in graphene, coupled by effectively incorporating phosphorus from the phytic acid into the carbon substrate. Meanwhile, basic magnesium carbonate decomposes during the heating process to produce gaseous substances, resulting in a large number of micro- and meso-holes. After the acid treatment of the carbonized material, the FeNi DSAs/N,P-PC is eventually harvested.

The microstructural features of the constructed catalyst were examined by SEM. As shown in Fig. 2 (a-b), there appear numerous ultra-thin carbon nanosheets with curling characteristics for the FeNi DSAs/N,P-PC, where show abundant macro- and meso-pores on the sheet-like structures. Such features can effectively reduce the resistance of material and shorten the interfacial distance of mass diffusion [28]. Further, the SEM (Fig. S1) and TEM, Fig. 2 (c-d) images further reveal the three-dimensional (3D) open porous structure with hierarchical interconnections. The unique architectures would greatly facilitate the accessibility of the active sites and thereby show the high-efficiency catalytic reactions [23].

High-resolution TEM images (Fig. 2 (e)) exhibit many clear lattice stripes with a inter-planar spacing distance of roughly 0.34 nm, corresponding to the (002) crystal planes of graphitic carbon [22]. The high-angle annular dark-field scanning transmission electron microscope (AC-STEM) image corrected for aberration is exhibited in Fig. 2 (f). As highlighted by the red circles, there exhibit a large number of independent bright spots, which are uniformly distributed on the carbon substrate, demonstrating the co-existence of Fe and Ni atomic sites in the prepared FeNi DSAs/N,P-PC. Also, there appear many small bright spots of the two dots in close proximity (labelled by the yellow cycle), implying the presence of adjacent FeNi diatomic sites [29]. In addition, the EDS spectrum (Fig. S2) and EDS mapping images (Fig. S3) show the homogeneous co-presence of N, P, Fe and Ni elements in the catalyst. These results indicate the effective doping of N and P into the carbon skeleton and the successful preparation of the Fe and Ni single-atom sites.
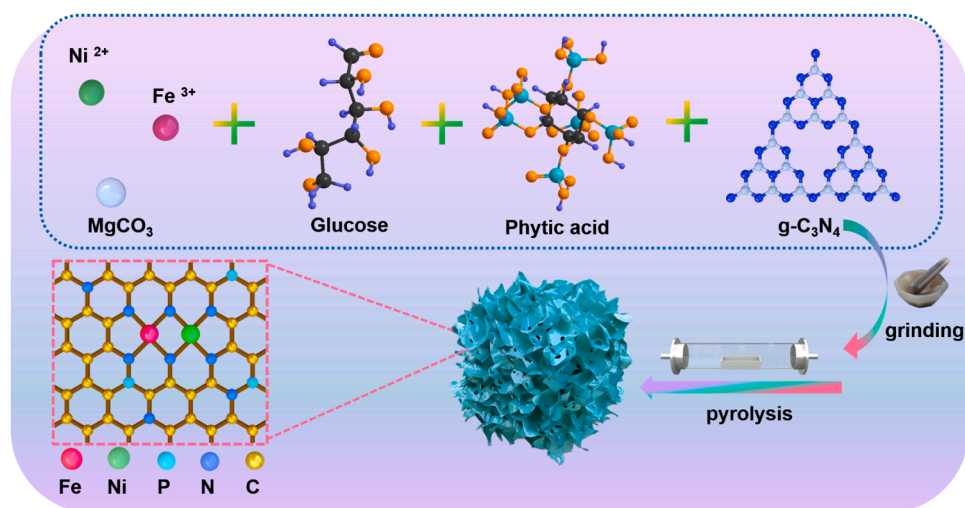
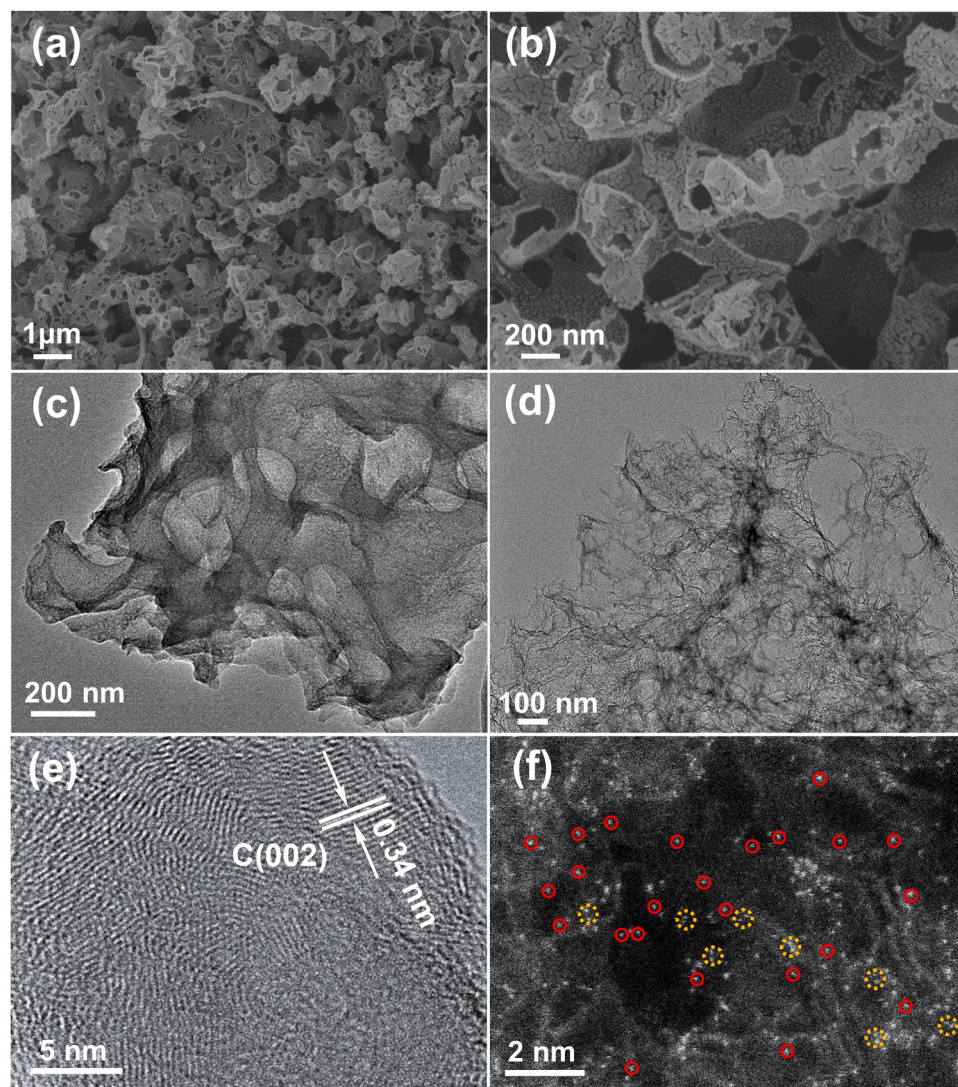**Fig. 1.** Schematic illustration for preparation of the FeNi DSAs/N,P-PC.

Fig. 2. (a, b) SEM, (c, d) TEM, and (e) HRTEM images of the FeNi DSAs/N,P-PC. (f) Aberration-corrected HAADF-STEM image.
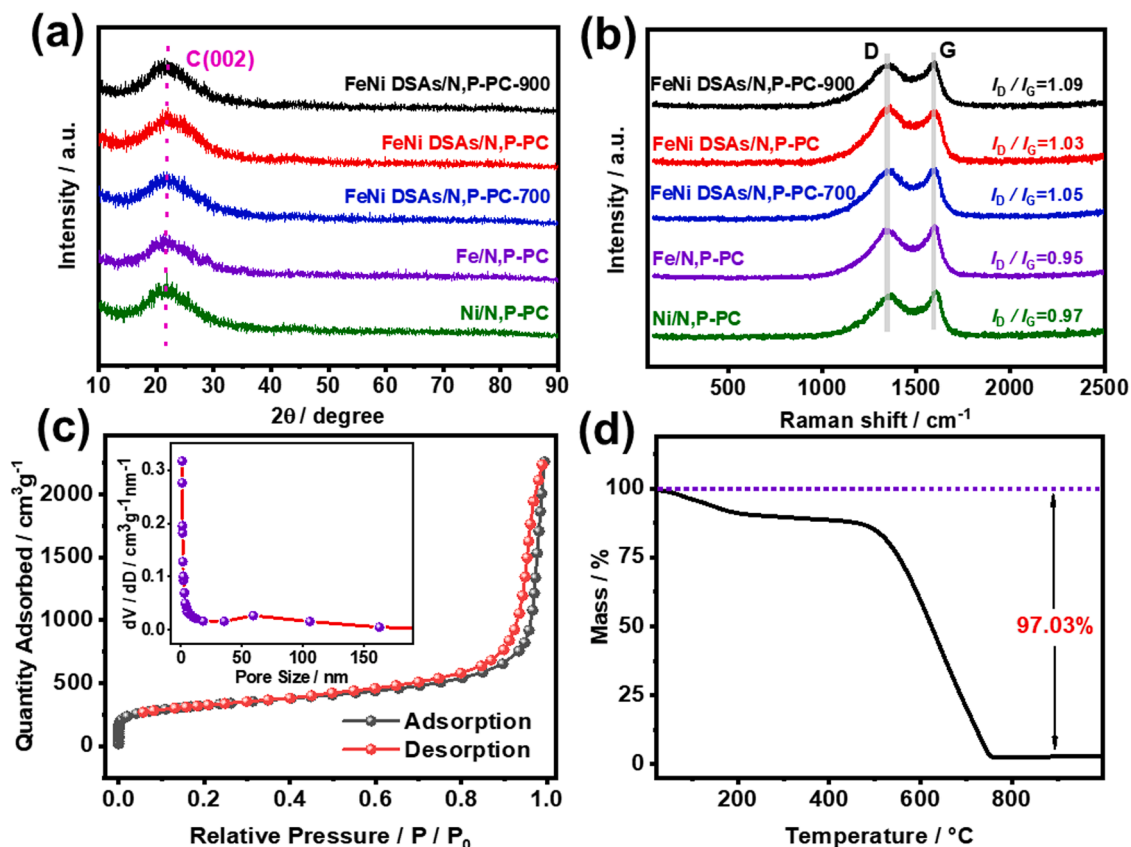
Fig. 3. (a) XRD patterns, (b) Raman spectra, and (c) nitrogen adsorption-desorption isotherms of the FeNi DSAs/N,P-PC. Inset in C displays the pore-size-distribution curve. (d) The corresponding TGA curve obtained in air atmosphere.

XRD analysis was conducted to rigorously examine the physical phase and crystal structure of the synthesized samples (Fig. 3 (a)). Plainly, only a significant broad diffraction peak is observed at around 22° for all of the samples, corresponding to the (002) crystalline planes of carbon [30], while there hardly shows any signal from the metal-based species. These observations are consistent with the AC-STEM analysis.

As seen from the Raman spectra in Fig. 3 (b), two characteristic peaks show up for all of the samples at approximately 1360 and 1590 cm^{-1}, which are associated with disordered sp^3 defective carbon (*D* band) and sp^2 graphitic carbon (*G* band) [31], respectively. What's more, the ratio of the two bands (i.e., I_D/I_G) is usually used to characterize the level of defects and graphitization, where defective carbon creates more active sites and graphitic carbon improves the electronic conductivity [32]. The I_D/I_G value is 1.03 for the FeNi DSAs/N,P-PC, which is located between those of the FeNi DSAs/N,P-PC-700 (1.05) and FeNi DSAs/N,P-PC-900 (1.09). These values indicate that the calcinated temperature plays an important role in regulating the balance between the defects and graphitization. Meanwhile, the I_D/I_G value of the FeNi DSAs/N,P-PC significantly outperforms those of the Fe/N,P-PC (0.95) and Ni/N,P-PC (0.97), indicating more structural defects formed and relatively less graphitization upon the introduction of the bimetallic atomic sites [33]. In the end, an appropriate I_D/I_G ratio is beneficial to the catalytic performance of the FeNi DSAs/N,P-PC.

The specific surface area and pore size characteristics of the FeNi DSAs/N,P-PC were scrutinized by the BET experiments (BJH, BSD Instrument 3 H-2000PS). As depicted in Fig. 3 (c), a type IV isotherm with a distinct hysteresis loop can be observed, indicating the co-presence of micro- and meso-pores, as further evidenced by the pore-size-distribution plot (inset in Fig. 3(c)). The BET specific surface area is calculated to be 1168.8 $m^2\ g^{-1}$ for the FeNi DSAs/N,P-PC, with a mean pore size of 11.36 nm. The large amount of gaseous material is generated by the decomposition of g-C_3N_4 and magnesium carbonate during the high-temperature pyrolysis procedure, integrated by the removal of magnesium oxide during the pickling process. The structural features would expose adequate active sites of the Fe and Ni atoms, providing more channels for interfacial mass transport and charge transfer, thereby enhancing the catalytic efficiency [28].

Thermogravimetric analysis (TGA) was performed to assess the metal content in the FeNi DSAs/N,P-PC. As illustrated in Fig. 3 (d), there unveils a certain degree of weight loss (~15%) when the temperature ascends from room temperature to 220 °C, owing to the removal of moisture remaining in the sample. The main weight loss is concentrated in a range of 500°C to 780°C, where the fast decomposition of carbon substrates in this interval leads to a dramatic weight loss, with the final oxide residue of 2.97%. According to inductively coupled plasma mass spectrometry (ICP-MS), the Fe and Ni contents are about 1.19% and 0.83%, respectively.

XPS analysis of the FeNi DSAs/N,P-PC was carefully carried out to gain a deeper insight of the surface chemistry and valence bonding of the catalyst. The full-scan XPS spectrum (Fig. 4 (a)) reveals the co-presence of C, N, P, O, Fe and Ni elements, consistent with the EDS test. Fig. 4 (b) shows the high-resolution C1s XPS region, which can be deconvoluted into the C-P (284.1 eV), C-C/C=C (284.7 eV), C-N (285.6 eV) and O-C=O (288.4 eV) [34,35]. The present C-P and C-N groups indicate the effective sequestration of N and P heteroatoms in porous carbon substrate.

The N1s XPS section (Fig. 4(c)) shows the pyridine-N (398.6 eV), M-N_x (399.0 eV), pyrrole-N (400.1 eV), graphite-N (401.1 eV), and oxide-N (404.2 eV) [29,36]. In general, different forms of nitrogen were found to effectively regulate the electronic architecture of the bimetal-doped carbon [37]. Specifically, the presence of pyridine-N has a positive
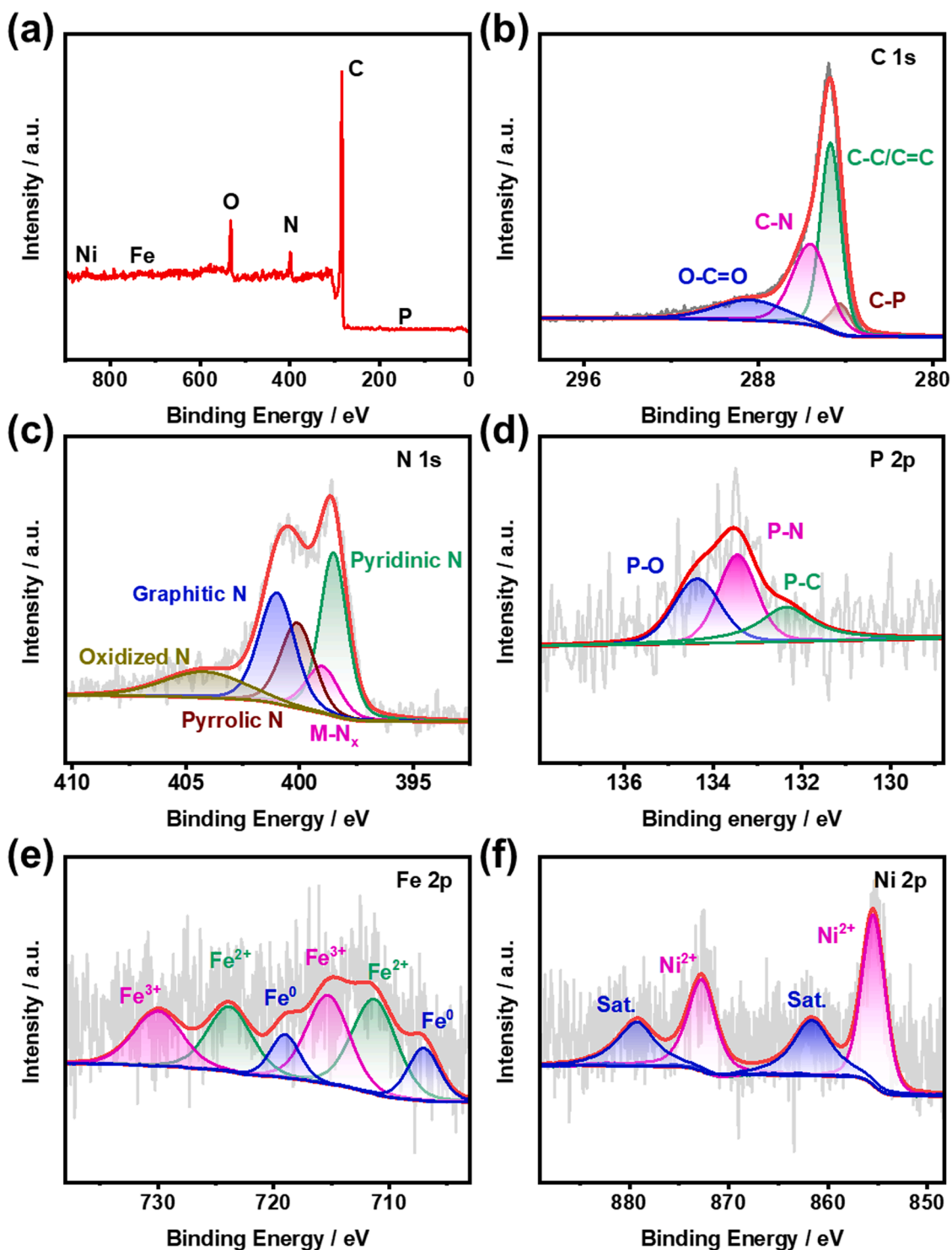
Fig. 4. (a) Survey, and high-resolution (b) C 1 s, (c) N 1 s, (d) P 2p, (e) Fe 2p and (f) Ni 2p XPS spectra of the FeNi DSAs/N,P-PC.

impact on improving the surface wettability and positive shift of the onset potential (E_{onset}) of the catalyst, while graphite-N can further increase the electrical conductivity and M-N$_x$ is important for improving the catalytic activity [38].

Fig. S4(a-b) shows the comparison of the nitrogen species levels of the catalysts (prepared at different calcinated temperature). Specifically, the FeNi DSAs/N,P-PC catalyst shows the higher total pyridine-N and graphite-N than the FeNi DSAs/N,P-PC-700 and FeNi DSAs/N,P-PC-900. As well, there displays a descend trend of the M-Nx contents as the pyrolyzed temperature rises from the FeNi DSAs/N,P-PC-700 to FeNi

DSAs/N,P-PC-900. In brief, the pyrolysis temperature plays an essential role on the type and content of the ultimate nitrogen species. It is worth noting that the pyridine-N is recognized as trapping sites for the carbon-supported metal species, reflecting its importance to form stable Fe-N$_x$ and Ni-N$_x$ coordinated structures in the FeNi DSAs/N,P-PC [39].

The P 2p XPS part (Fig. 4(d)) shows three peaks with binding energies of 132.1 eV, 133.2 eV and 134.3 eV corresponding to the P-C, P-N and P-O groups [40], respectively, further indicating the successful doping of N and P atoms into the carbon substrate. Their double doping induces an asymmetric charge density, which effectively increases the

charge leaving domain of the surrounding carbon atoms, thereby promoting the 4e⁻ pathway required for the ORR [41]. Meanwhile, the local electronically engineered configuration of the metal active center has a lower energy barrier for the adsorption/desorption of oxygen-containing intermediates, which would greatly accelerate the ORR kinetics and enhances the ORR catalytic performance [42].

As shown in the Fe 2p segment (Fig. 4 (e)), the peaks at 707.0, 710.8 and 714.8 eV are associated with the Fe^0, Fe^{2+} and Fe^{3+} species of Fe $2p_{3/2}$, while those at 719.0, 723.3 and 730.5 eV are assigned to the Fe^0, Fe^{2+} and Fe^{3+} species of Fe $2p_{1/2}$ [26,43], where the high valence of Fe

is the predominance. Also, the Ni 2p XPS section (Fig. 4 (f)) exhibits the peak at 855.4 eV stemmed from Ni^{2+} species of Ni $2p_{3/2}$, while the one at 872.7 eV originated from Ni^{2+} species of Ni $2p_{1/2}$, combined by showing two broad satellite peaks at 861.4 and 879.3 eV [44,45]. In a word, these observations demonstrate the main predominance of the Ni^{2+} species in the sample. Notably, when Ni and Fe coexist, the binding energy of the Fe 2p state shows a negative shift trend while that of the Ni 2p state shows a positive shift trend (Fig. S5(a-b)), further suggesting that the interactions between Ni and Fe atoms can effectively modulate the electronic structure of the FeNi DSAs/N,P-PC. The interactions
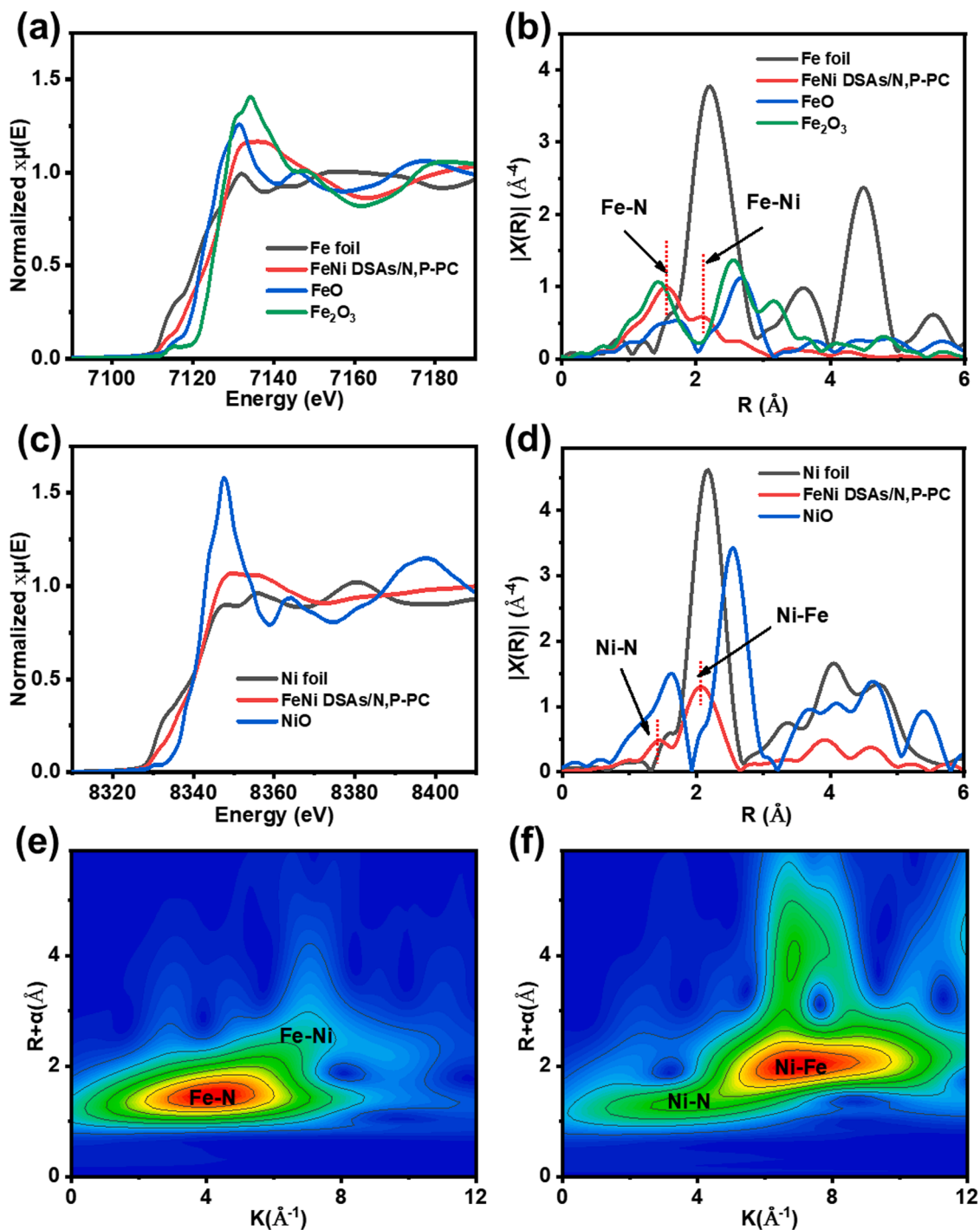

Fig. 5. (a) Fe K-edge XANES and (b) Fourier-transform EXAFS spectra of the FeNi DSAs/N,P-PC and reference samples. (c) Ni K-edge XANES and (d) Fourier-transform EXAFS spectra of the FeNi DSAs/N,P-PC and reference samples. (e) Fe and (f) Ni Wavelet transforms of these k2-weighted χ(k) signals of the FeNi DSAs/N,P-PC.

between Fe and Ni atoms act as an intrinsic driving force for the formation of Fe-Ni atomic pairs, thus providing optimal active sites and facilitating the adsorption/desorption of reactive molecules and reaction intermediates [4].

Advanced XAFS technology was further employed to elucidate the local structural features of Fe and Ni atoms in the FeNi DSAs/N,P-PC and compared with the related standards. Fig. 5 (a) presents the normalized X-ray absorption near edge structure (XANES) profile of the Fe K-edge. The energy absorption thresholds of Fe atoms in the FeNi DSAs/N,P-PC lie between Fe foil (0) and FeO (+2), which indicate that the valence state of Fe in the samples is close to +2 valence. Meanwhile, the relevent

Fe K-edge Fourier transform k2-weighted extended X-ray absorption fine structure (FT-EXAFS) spectra (Fig. 5 (b)) reveals that a main peak exists near 1.5 Å, corresponding to the Fe-N interactions. When compared to the Fe foil, the FeNi DSAs/N,P-PC has no detectable presence of the Fe-Fe scattering path at 2.20 Å, indicating the successful separation of the Fe atoms. Notably, a shoulder peak corresponds to the Fe-Ni scattering peak at 2.05 Å, confirming the formation of the Fe-Ni atomic pairs.

Similarly, Fig. 5 (c) shows the Ni K side XANES profile of FeNi DSAs/ N,P-PC, from which it can be observed that the oxidation state of Ni increases as the energy increase, and the valence state of Ni in the sample is between 0 and +2 valence. For the Ni K-edge FT-EXAFS
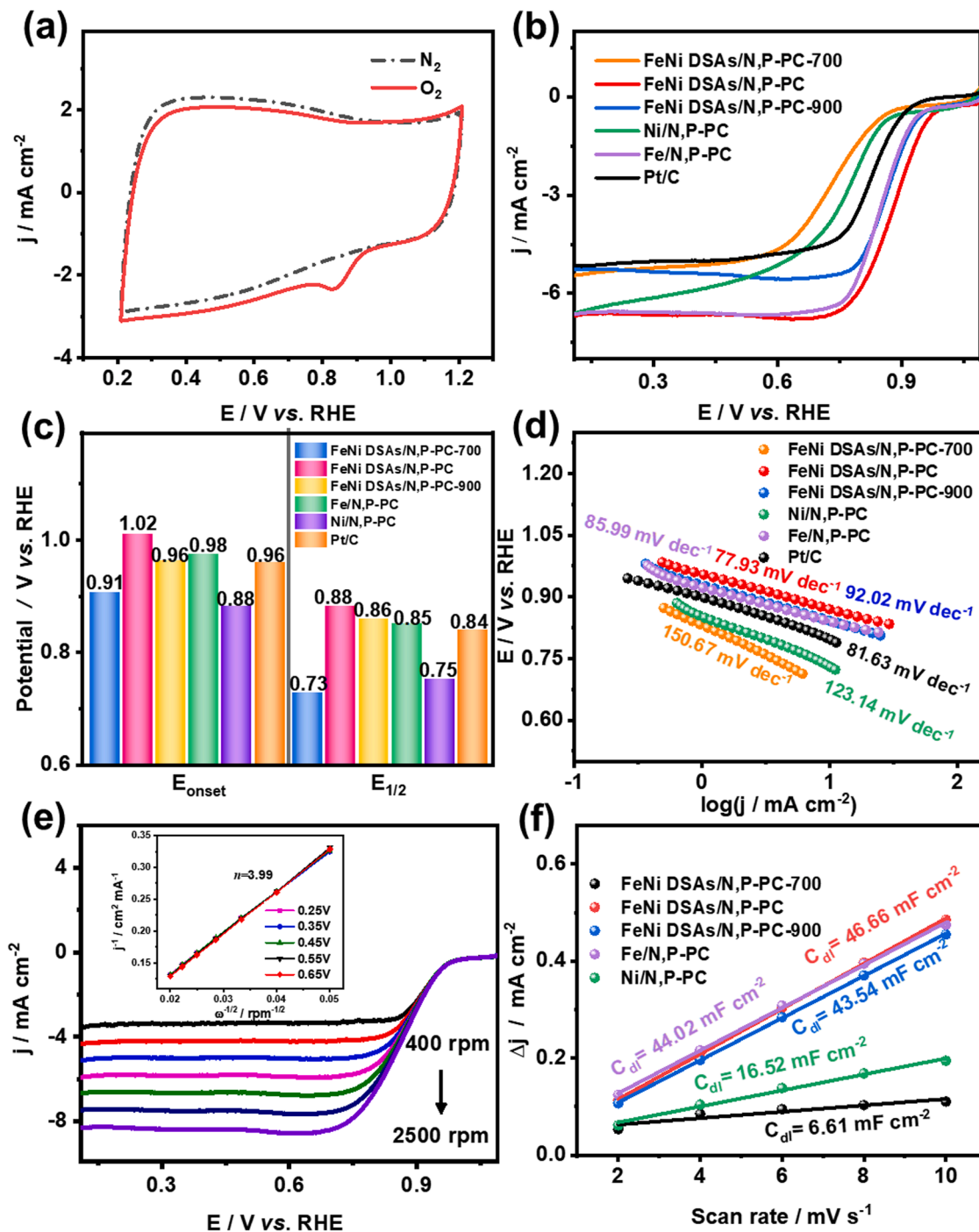

Fig. 6. (a) CV curves recorded in the N_2- or O_2-saturated 0.1 M KOH electrolyte at 50 mV s^{-1}. (b) LSV plots of the catalysts acquired in the O_2-saturated solution at 1600 rpm and 10 mV s^{-1}. (c) The corresponding E_{onset} and $E_{1/2}$ values. (d) Tafel plots. (e) LSV curves of the FeNi DSAs/N,P-PC at different rotation rates. Inset in E displays the K-L plots at different potentials. (f) The C_{dl} values.

spectra of the FeNi DSAs/N,P-PC (Fig. 5 (d)), the characteristic peaks corresponding to the Ni-N interactions and Ni-Fe scattering paths, can likewise be noted, while there is no characteristic peaks corresponding to the Ni-Ni scattering paths in the Ni foil. In addition, Fig. 5 (e-f) demonstrate the wavelet transform (WT) images of the Fe and Ni of the FeNi DSAs/N,P-PC, coupled by showing equally no signals of Fe foils (Fe-Fe) and nickel foils (Ni-Ni) (Fig. S6), further confirming the atomically dispersed diatomic sites of Fe and Ni, as well as the formation of the metal-N structure, which are consistent with the reported bimetallic sites [30].

3.2. Electrochemical measurements

The ORR performance of the investigated catalyst was rigorously tested at room temperature by using a rotating disc electrode in the O_2- or N_2-saturated 0.1 M KOH electrolyte. Fig. 6 (a) shows the cyclic voltammetry (CV) curves, where the FeNi DSAs/N,P-PC shows a clear reduction peak under the O_2-saturated conditions, while no other peak appears in the N_2 saturated environment, suggesting its excellent ORR performance [46].

LSV test was used to further assess the ORR catalytic performance of all the catalysts. Fig. 6 (b-c) exhibits the corresponding LSV curves and their comparison in terms of the onset potential (E_{onset}) and half-wave potential ($E_{1/2}$). Briefly, the FeNi DSAs/N,P-PC catalyst exhibits the most positive E_{onset} (1.02 V) and $E_{1/2}$ (0.88 V), exceeding the FeNi DSAs/N,P-PC-700 ($E_{onset} = 0.91$ V; $E_{1/2} = 0.73$ V), FeNi DSAs/N,P-PC-900 ($E_{onset} = 0.96$ V; $E_{1/2} = 0.86$ V) and commercial Pt/C ($E_{onset} = 0.96$ V; $E_{1/2} = 0.84$ V). Moreover, these catalysts are comparable to or even surpass many of the earlier reported carbon loaded transition metal catalysts (Table S1). It is worth noting that the ORR performance of the FeNi DSAs/N,P-PC is also superior to those of the Fe/N,P-PC ($E_{onset} = 0.98$ V; $E_{1/2} = 0.85$ V) and Ni/N,P-PC ($E_{onset} = 0.88$ V; $E_{1/2} = 0.75$ V). Impressively, the presence of adjacent Ni sites enhances the Fe 3d electron leaving domain, and accelerates the interfacial electron transfer between the catalyst and the oxygen-containing intermediates, thus enhancing the ORR catalytic performance [47].

The Tafel slope was obtained by further analysis of the LSV data, which can be used to assess the catalytic kinetics of all the prepared catalysts and Pt/C [48]. As shown in Fig. 6 (d), the FeNi DSAs/N,P-PC has the lowest Tafel slope value (77.93 mV dec^{-1}), indicating the enhanced ORR catalytic kinetics relative to the other control samples. The ORR activity of the prepared FeNi DSAs/N,P-PC is comparable to most of the reported diatomic metal-site catalysts in terms of the E_{onset}, $E_{1/2}$, and Tafel slopes (Table S2).

In order to deeply investigate the ORR mechanism of the FeNi DSAs/N,P-PC, LSV tests were carried out at various rotation speeds (i.e., 400–2500 rpm). As seen in Fig. 6 (e), all of the LSV curves have a

constant starting potential, and the limiting current density increases with velocity in a regular manner. The matching Koutecky-Levich (K-L) graph shows a well linear relationship, and harvests an average electron transfer number of approximately 3.99. In addition, the rotating ring disc electrode (RRDE) tests show that the H_2O_2 yield of the FeNi DSAs/N,P-PC remains below 11.69 wt% over a potential range of 0.2–0.8 V, with a corresponding electron transfer number of 3.87–4.0 (Fig. S7). The efficient direct reduction of O_2 to H_2O is reflected, further verifying that the ORR follows an efficient 4e- reduction pathway.

The ECSA is an important basis for characterizing the number of accessible active sites and their intrinsic activity of a catalyst, which is usually linearly correlated with the double-layer capacitance (C_{dl}) [49]. The C_{dl} values were calculated by measuring the CV curves in the non-Faraday region at different scan rates (Fig. S8). As Fig. 6 (f) depicts, the C_{dl} value of the FeNi DSAs/N,P-PC is about 46.66 mF cm^{-2}, which is superior to those of the FeNi DSAs/N,P-PC-700 (6.61 mF cm^{-2}), FeNi DSAs/N,P-PC-900 (43.54 mF cm^{-2}), Fe/N,P-PC (44.02 mF cm^{-2}) and Ni/N,P-PC (16.52 mF cm^{-2}). These data indicate that the bimetal single atoms can provide more accessible active sites, finally enhancing the ORR performance [50,51].

Apart from the good ORR performance, the longevity of the catalyst's operational stability is also critical to realize the practical application of the catalyst [52]. As shown in Fig. 7 (a), the LSV plots of the FeNi DSAs/N,P-PC shows good stability with a negative shift of only 14 mV in the $E_{1/2}$ after scanning for 2000 cycles. Meanwhile, the chronoamperometric results (Fig. 7 (b)) show that the FeNi DSAs/N,P-PC can still maintain 94.1% of its initial value after operating for 10 h, while Pt/C drops down to 68.6% of its original value, further verifying its excellent long-term operational stability. These superior properties are mainly due to the precise modulation of the electronic structure around the metal atom as well as the carbon atom doped by the N and P atoms, which effectively stabilizes the metal sites and improves the intrinsic activity [53]. Fig. S9 exhibits the correlated LSV curves, the overpotential of the FeNi DSAs/N,P-PC is 409 mV at a current density of 10 mA cm^{-2}, which shows the limited OER catalytic performance as compared to the overpotential of 265 mV for the RuO_2 catalyst.

3.3. DFT simulations

In order to elucidate the intrinsic ORR catalysis mechanism of the FeNi DSAs/N,P-PC in more depth, we have further explored its free energy, charge density difference, and projected density of states (PDOS) in the oxygen electrocatalytic reaction by means of the DFT calculations. At the beginning of the calculations, the constructed model (Fig. S10) was first optimized of Fe single atoms/N,P-PC(a), Ni single atoms/N,P-PC (b), and FeNi DSAs/N,P-PC (c). It reflects that inserting P adjacent to Fe-N (site 10), Ni-N (site 8) and FeNi-N (site 16) atoms,
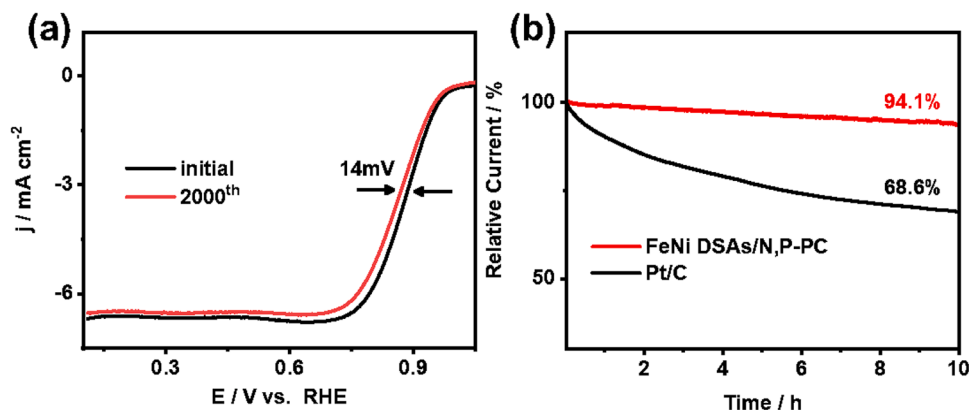

Fig. 7. (a) LSV curves of the FeNi DSAs/N,P-PC before and after scanning for 2000 cycles in the O_2-saturated solution at 10 mV s^{-1}. (b) Chronoamperometric curves of the catalysts collected at 0.6 V with a rotation rate of 1600 rpm.

results in the lowest energy of the whole bulk system. And since the dangling bonds on the P atoms are easily neutralized by the O atoms, we chose the structure in the presence of P-O bonds for the simulations in the subsequent calculations. Fig. S11(a-b) show the ORR reaction energy levels of monoatomic Ni and the adsorption transfer scheme of the ORR-catalyzed intermediate O* in the monoatomic Fe/Ni system, and we find that Ni atoms adsorb weakly on the ORR intermediated O, catalyzing the ORR reaction with a low activity. Furthermore, the O* adsorbed on the Ni migrates to the Fe atom very easily in the FeNi dual atomic system, indicating that the Fe is the active center for the catalytic ORR reaction.

Fig. 8 (a) provides a diagram of the ORR mechanism of the FeNi DSAs/N,P-PC under alkaline conditions, involving four intermediate states of the ORR-catalyzed reaction. The rate-determining step (RDS) is the crucial for evaluating the catalytic activity of a catalyst at a specific site, and a larger energy difference in the RDS represents a larger over potential. Gibbs free energy change curves (Fig. 8(b)) were calculated for each reaction step of the ORR at equilibrium potential (U = 1.23 V). The RDS for both the P-O/FeNi DSAs/N,P-PC and P-O/Fe/N,P-PC models is the last step, which generates H_2O molecules from OH* intermediates. The reaction energy barrier of the FeNi diatomic site is 0.81 eV, which is lower than that of the monoatomic Fe site (1.04 eV), indicating that the coupling of the Ni and Fe monoatomic sites can effectively reduce the theoretical over potential of the system, which is more favorable for the ORR reaction. In addition, the surface of Fe atoms in the FeNi diatomic sitesis prone to adsorb O* or HO* in the alkaline system. Calculations show that the overpotential of the whole system is further reduced after such adsorption, which is good for the ORR.

A differential charge density analysis (Fig. 8 (c)) was performed to reveal the charge transfer trend on the P-O/FeNi DSAs/N,P-PC model. For the Fe and FeNi sites, the charge is transferred from the Fe center to the neighboring N atoms. And the symmetry of the charge distribution is effectively broken due to the coupling of the Ni single atom to the Fe center, resulting in a greater charge transfer in the system and lowering the reaction energy barriers, which reflects the stronger interactions between the bimetallic metal atoms [47]. Finally, in order to gain more insight into how the FeNi atomic sites affects the ORR performance, partial density of states (PDOS) and d-band center analysis (Fig. 8 (d)) were further implemented. The simulation analysis reveals that a significant negative shift of the d-band center occurs in the FeNi model, in comparison to the Fe counterpart. It means that the ability to replenish the antibonding orbitals filled with electrons faster throughout the system and weaken the dynamic interactions of the active site with the intermediates is more advantageous to the catalytic reaction progress [54].

3.4. Application of Zn-air battery

Liquid rechargeable zinc-air battery based on the FeNi DSAs/N,P-PC was assembled to verify the applicability. Specifically, the FeNi DSAs/N,P-PC loaded on carbon paper was used as the air cathode, a polished zinc plate as the anode, and the 6.0 M KOH solution containing 0.2 M Zn $(CH_3COO)_2$ as the electrolyte. Similarly, a zinc-air cell based on a Pt/C + RuO_2 hybrid catalyst was behaved as a control. The FeNi DSAs/N,P-PC derived battery has an open circuit voltage of ~1.508 V (Fig. 9 (a)), which is higher than that of the Pt/C + RuO_2 (~1.440 V). As shown in Fig. 9 (b), two zinc-air batteries connected in series are able to successfully lighting two light emitting diodes (~3 V) connected in parallel. Subsequently, the home-made battery was tested for constant current discharge at different current densities (Fig. 9 (c)). Concisely, there maintains a relatively smooth discharge plateau even at a higher current
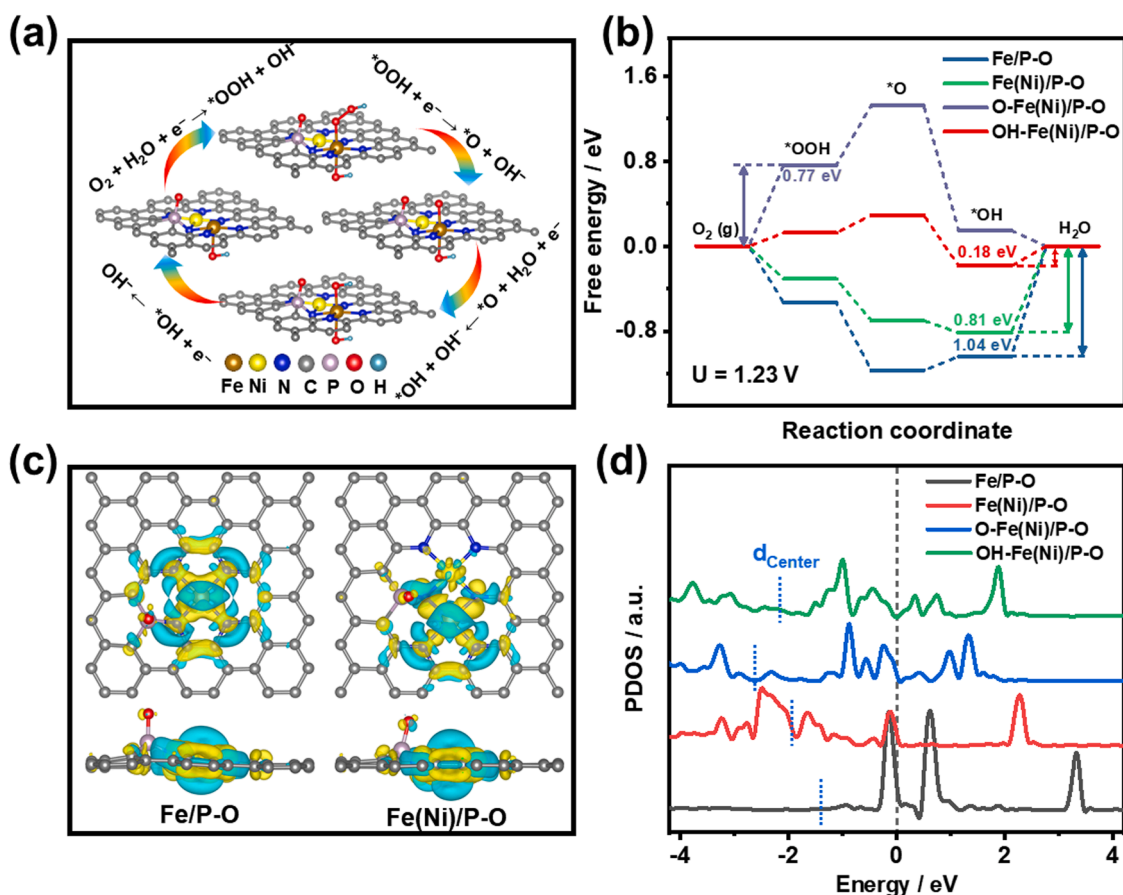

Fig. 8. (a) Mechanistic diagram of the ORR. (b) Free energy step diagram of the ORR (U = 1.23 V). (b) Differential charge density diagrams of the Fe/P-O and Fe (Ni)/P-O. (d) Calculated PDOS profiles.
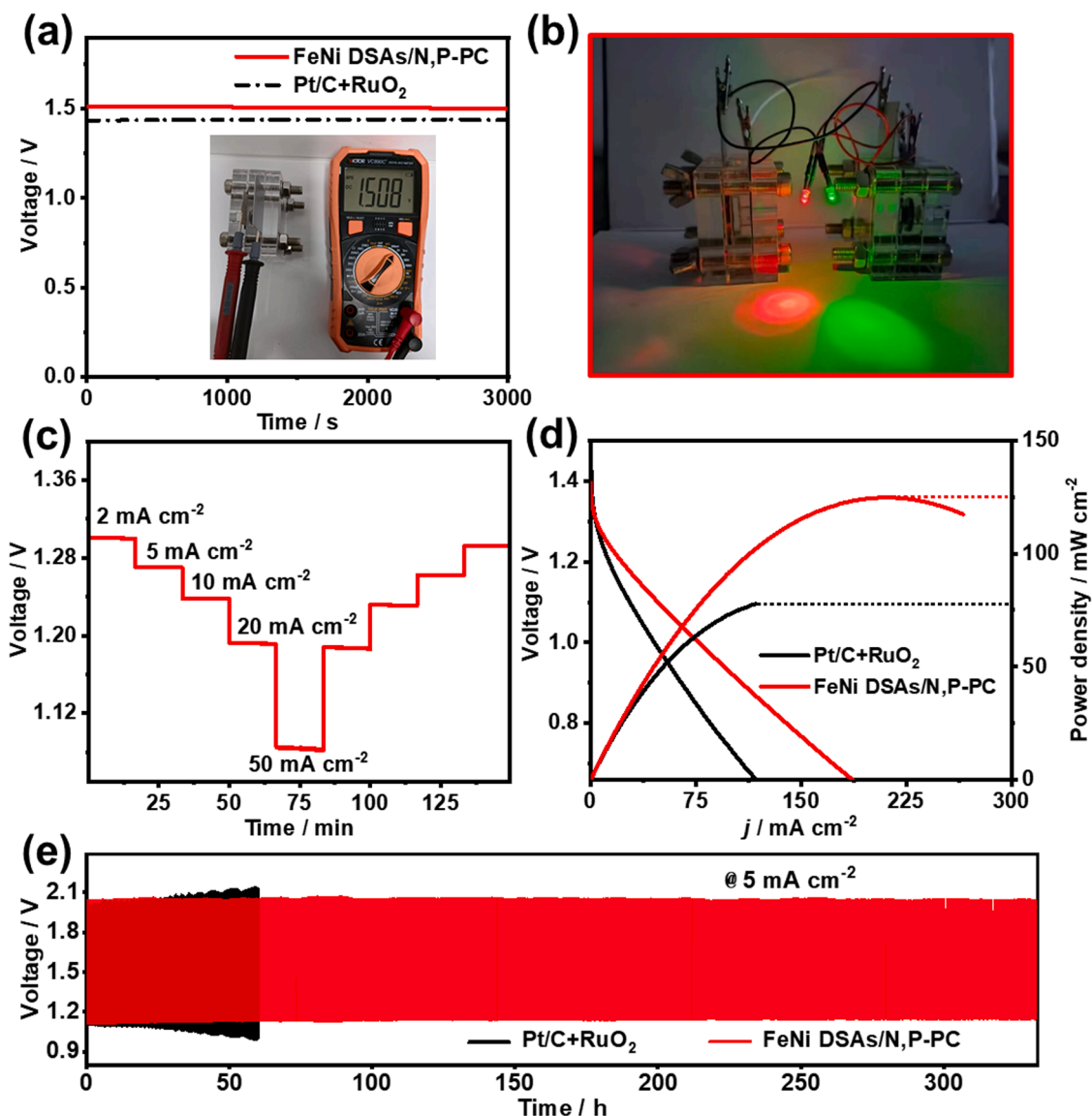
Fig. 9. (a) Open-circuit voltages, and (b) photograph of the two-series-connected Zn-air battery based on the FeNi DSAs/N,P-PC for light-emitting diode (3 V). (c) Discharge voltage change with the current densities and time. (d) Polarization and power density curves of the investigated catalysts. (e) Long-term galvanostatic charge-discharge cycling curves at 5 mA cm^{-2}.

density of 50 mA cm^{-2}, exhibits good reversibility and multiplicative capability.

More notably, Fig. 9 (d) provides the home-made cell discharge polarization curve and power density plot with a peak power density of 124.73 mW cm^{-2}, which far exceeds that of the Pt/C + RuO$_2$ based counterpart (77.92 mW cm^{-2}). Finally, when the FeNi DSAs/N,P-PC based zinc-air cell was charged and discharged for 330 h at 5 mA cm^{-2} (Fig. 9 (e)). Apparently, the voltage difference increases slightly from 0.899 V to 0.938 V. In contrast, the Pt/C + RuO$_2$ derived cells exhibit unacceptable charge and discharge voltage gaps after only cycling for 70 h. These results demonstrate the promising long-term operational stability of the FeNi DSAs/N,P-PC based batteries and the feasibility of future practical applications.

The remarkable ORR catalytic performance of the FeNi DSAs/N,P-PC is mainly attributed to the following aspects: (1) The strong synergistic effect between the bimetallic atoms in the catalyst and the adjacent Ni sites can alleviate the electron localization of Fe and promote the electron delocalization of Fe 3d orbitals, thus accelerating the interfacial electron transport for the ORR [54,55]. (2) The N,P double-doped configuration can optimize the charge distribution and

electronegativity of the metal active center, which is more conducive to lowering the adsorption/desorption energy barrier of the oxygen-containing intermediates and enhancing the ORR kinetics, thus improving the ORR performance [42,56]. (3) The prepared FeNi DSAs/N,P-PC has an open three-dimensional porous structure and a larger ECSA of up to 1168.8 m^2 g^{-1}, which is more beneficial for the interfacial mass diffusion as well as the exposure of more bimetallic sites, eventually enhancing the catalytic efficiency [28,57].

4. Conclusions

In conclusion, the FeNi DSA/N,P-PC developed by a simple pyrolysis strategy showed significant ORR activity ($E_{1/2} = 0.88$ V) and stability in alkaline media. Moreover, its application in a home-made zinc-air battery exhibited greater peak-power density (124.73 mW cm^{-2}) and stable long-term charge/discharge cycling stability (330 h). The XANES and DFT studies identify FeNi diatomic site as well as metal-nitrogen structures with high intrinsic catalytic activity. The strong interactions between the bimetallic atoms and effective modulation of the active center by the doped heteroatom play a crucial role in the outstanding

performance of the catalyst. In parallel, the hierarchical porous structure and the N/P double doping configuration of the catalyst account for the boosted ORR, integrated with the synergistic effect between the FeNi dual metal sites. This work provides a viable strategy for development of diatomic catalysts suitable for high-efficiency energy conversion and storage devices.

CRediT authorship contribution statement

Lu Zhang: Methodology, Formal analysis, Writing – original draft. **Dong-Hui Wu:** Formal analysis, Data curation. **Mahmood Ul Haq:** Methodology, Investigation. **Jiu-Ju Feng:** Methodology, Investigation. **Fa Yang:** Validation, Writing – review & editing. **Ai-Jun Wang:** Validation, Writing – review & editing.

Declaration of Competing Interest

The authors declare that they have no known competing financial interests or personal relationships that could have appeared to influence the work reported in this paper.

Data availability

Data will be made available on request.

Appendix A. Supporting information

Supplementary data associated with this article can be found in the online version at doi:10.1016/j.apcatb.2024.123991.

References

[1] B. Wu, H.B. Meng, D.M. Morales, F. Zeng, J.J. Zhu, B. Wang, M. Risch, Z.J. Xu, T. Petit, Nitrogen-rich carbonaceous materials for advanced oxygen electrocatalysis: synthesis, characterization, and activity of nitrogen sites, Adv. Funct. Mater. 32 (2022) 2204137.
[2] H. Hu, J.J. Wang, B.F. Cui, X.R. Zheng, J.G. Lin, Y.D. Deng, X.P. Han, Atomically dispersed selenium sites on nitrogen-doped carbon for efficient electrocatalytic oxygen reduction, Angew. Chem. Int. Ed. 61 (2022) e202114441.
[3] L. Zhang, Y.X. Zhu, Z.C. Nie, Z.Y. Li, Y. Ye, L.H. Li, J. Hong, Z.H. Bi, Y.T. Zhou, G. Z. Hu, Co/MoC nanoparticles embedded in carbon nanoboxes as robust trifunctional electrocatalysts for a zn-air battery and water wlectrocatalysis, ACS Nano 15 (2021) 13399–13414.
[4] G. Yasin, S. Ali, S. Ibraheem, A. Kumar, M. Tabish, M.A. Mushtaq, S. Ajmal, M. Arif, M.A. Khan, A. Saad, L. Qiao, W. Zhao, Simultaneously engineering the synergistic-effects and coordination-environment of dual-single-atomic iron/cobalt-sites as a bifunctional oxygen electrocatalyst for rechargeable zinc-air batteries, ACS Catal. 13 (2023) 2313–2325.
[5] L.L. Liu, D.H. Wu, L. Zhang, J.J. Feng, A.J. Wang, FeCo alloy entrapped in N-doped graphitic carbon nanotubes-on-nanosheets prepared by coordination-induced pyrolysis for oxygen reduction reaction and rechargeable zn-air battery, J. Colloid Interface Sci. 639 (2023) 424–433.
[6] Y.T. He, X.X. Yang, Y.S. Li, L.T. Liu, S.W. Guo, C.Y. Shu, F. Liu, Y.N. Liu, Q. Tan, G. Wu, Atomically dispersed Fe–Co dual metal sites as bifunctional oxygen electrocatalysts for rechargeable and flexible zn–air batteries, ACS Catal. 12 (2022) 1216–1227.
[7] B. Wang, J. Tang, X.H. Zhang, M. Hong, H.K. Yang, X. Guo, S. Xue, C.C. Du, Z. X. Liu, J.H. Chen, Nitrogen doped porous carbon polyhedral supported Fe and Ni dual-metal single-atomic catalysts: template-free and metal ligand-free sysnthesis with microwave-assistance and d-band center modulating for boosted ORR catalysis in zinc-air batteries, Chem. Eng. J. 437 (2022) 135295.
[8] H.W. Zhang, X. Jin, J.M. Lee, X. Wang, Tailoring of active sites from single to dual atom sites for highly efficient electrocatalysis, ACS Nano 16 (2022) 17572–17592.
[9] M.T. Zhang, H. Li, J.X. Chen, F.X. Ma, L. Zhen, Z.H. Wen, C.Y. Xu, High-loading Co single atoms and clusters active sites toward enhanced electrocatalysis of oxygen reduction reaction for high-performance zn–air battery, Adv. Funct. Mater. 33 (2022) 2209726.
[10] R.Z. Li, D.S. Wang, superiority of dual-atom catalysts in electrocatalysis: one step further than single-atom catalysts, Adv. Energy Mater. 12 (2022) 2103564.
[11] T. Gan, D. Wang, Atomically dispersed materials: ideal catalysts in atomic era, Nano Res. 17 (2023) 18–38.
[12] X.H. Liu, F. Zhao, L. Jiao, T.W. Fang, Z.Y. Zhao, X.F. Xiao, D.Y. Li, K. Yi, R.J. Wang, X. Jia, Atomically dispersed Fe/N4 and Ni/N4 sites on separate-sides of porous carbon nanosheets with janus structure for selective oxygen electrocatalysis, Small 11 (2023) e2300289.
[13] Y.F. Hu, Z.S. Li, B.L. Li, C.L. Yu, Recent progress of diatomic catalysts: general design fundamentals and diversified catalytic applications, Small 18 (2022) 2203589.
[14] H. Liu, L.Z. Jiang, J. Khan, X.X. Wang, J.M. Xiao, H.D. Zhang, H.J. Xie, L.N. Li, S. Y. Wang, L. Han, Decorating single-atomic Mn sites with FeMn clusters to boost oxygen reduction reaction, Angew. Chem., Int. Ed. 62 (2023) e202214988.
[15] J.J. Wang, C.X. Zhao, J.N. Liu, Y.W. Song, J.Q. Huang, B.Q. Li, Dual-atom catalysts for oxygen electrocatalysis, Nano Energy 104 (2022) 107927.
[16] Z.Y. Wang, C. Wang, Y.D. Hu, S. Yang, J. Yang, W.X. Chen, H. Zhou, F.Y. Zhou, L. X. Wang, J.Y. Du, Y.F. Li, Y. Wu, Simultaneous diffusion of cation and anion to access N, S co-coordinated Bi-sites for enhanced CO2 electroreduction, Nano Res. 14 (2021) 2790–2796.
[17] Y.T. He, Y.F. Jia, B.Z. Yu, Y. Wang, H.T. Li, Y.N. Liu, Q. Tan, Heteroatom coordination regulates iron single-atom-catalyst with superior oxygen reduction reaction performance for aqueous zn-air battery, Small 19 (2023) e2206478.
[18] X. Liang, N.H. Fu, S.C. Yao, Z. Li, Y.D. Li, The progress and outlook of metal single-atom-site catalysis, J. Am. Chem. Soc. 144 (2022) 18155–18174.
[19] H.B. Yin, P.F. Yuan, B.A. Lu, H.C. Xia, K. Guo, G.G. Yang, G. Qu, D.P. Xue, Y.F. Hu, J.Q. Cheng, S.C. Mu, J.N. Zhang, Phosphorus-driven electron delocalization on edge-type FeN4 active sites for oxygen reduction in acid medium, ACS Catal. 11 (2021) 12754–12762.
[20] M.W. Li, Q.L. Ye, S.Y. Hou, J.L. Yang, B. Chi, Y.J. Deng, X.L. Tian, Fluorine and phosphorus atoms cooperated on an N-doped 3D porous carbon network for enhanced ORR performance toward the zinc–air batteries, J. Mater. Chem. A 11 (2023) 8730–8738.
[21] Y.T. Zhou, Y.K. Liu, Z.L. Wang, C.Y. Li, Z.Y. Wang, S. Zhang, C. Deng, Fe-Co dual atomic doublets on N, P codoped carbon as active sites in the framework of heterostructured hollow fibers towards high-performance flexible zn-air battery, Energy Storage Mater. 59 (2023) 102772.
[22] S.Y. Lin, L.X. Xia, Y. Cao, H.L. Meng, L. Zhang, J.J. Feng, Y. Zhao, A.J. Wang, Electronic regulation of ZnCo dual-atomic active sites entrapped in 1D@2D hierarchical N-doped carbon for efficient synergistic catalysis of oxygen reduction in zn-air battery, Small 18 (2022) e2107141.
[23] C.G. Hu, L.M. Dai, Carbon-based metal-free catalysts for electrocatalysis beyond the ORR, Angew. Chem., Int. Ed. 55 (2016) 11736–11758.
[24] W.J. Tian, H.Y. Zhang, X.G. Duan, H.Q. Sun, G.S. Shao, S.B. Wang, Porous carbons: structure-oriented design and versatile applications, Adv. Funct. Mater. 30 (2020) 1909265.
[25] L. Wang, J. Wu, S. Wang, H. Liu, Y. Wang, D. Wang, The reformation of catalyst: From a trial-and-error synthesis to rational design, Nano Res. 18 (2023) 23–64.
[26] M.T. Chen, Z.X. Huang, X. Ye, L. Zhang, J.J. Feng, A.J. Wang, Caffeine derived graphene-wrapped Fe3C nanoparticles entrapped in hierarchically porous N-C nanosheets for boosting oxygen reduction reaction, J. Colloid Interface Sci. 637 (2023) 216–224.
[27] S.F. Ji, Y.J. Chen, X.L. Wang, Z.D. Zhang, D.S. Wang, Y.D. Li, Chemical synthesis of single atomic site catalysts, Chem. Rev. 120 (2020) 11900–11955.
[28] X.G. Li, Y.L. Zhao, Y.G. Yang, S.Y. Gao, A universal strategy for carbon–based ORR–active electrocatalyst: one porogen, two pore–creating mechanisms, three pore types, Nano Energy 62 (2019) 628–637.
[29] J. Yan, M. Tian, R.H. Shi, T.Y. Gu, K. Zeng, J.H. Zhou, Q. Zhang, M.H. Rümmeli, R. Z. Yang, Enhanced dual atomic Fe-Ni sites in N-doped carbon for bifunctional oxygen electrocatalysis, Mater. Today Energy 30 (2022) 101171.
[30] D.S. Yu, Y.C. Ma, F. Hu, C.C. Lin, L.L. Li, H.Y. Chen, X.P. Han, S.G. Peng, Dual-sites coordination engineering of single atom catalysts for flexible metal–air batteries, Adv. Energy Mater. 11 (2021) 2101242.
[31] S.Y. Lin, L.X. Xia, L. Zhang, J.J. Feng, Y. Zhao, A.J. Wang, Highly active Fe centered FeM-N-doped carbon (M=Co/Ni/Mn): a general strategy for efficient oxygen conversion in zn–air battery, Chem. Eng. J. 424 (2021) 130559.
[32] Z.P. Yu, C.W. Si, A.P. LaGrow, Z.X. Tai, W.A. Caliebe, A. Tayal, M.J. Sampaio, J.P. S. Sousa, I. Amorim, A. Araujo, L.J. Meng, J.L. Faria, J.Y. Xu, B. Li, L.F. Liu, Iridium–iron diatomic active sites for efficient bifunctional oxygen electrocatalysis, ACS Catal. 12 (2022) 9397–9409.
[33] D.S. Wang, H. Xu, P.X. Yang, X.Y. Lu, J.Y. Ma, R.P. Li, L.H. Xiao, J.Q. Zhang, M. Z. An, Fe–N4 and Co–N4 dual sites for boosting oxygen electroreduction in zn–air batteries, J. Mater. Chem. A 9 (2021) 13678–13687.
[34] D. Wu, S. Wu, G.L. Zhang, C.Y. Hui, D.J. Cao, S.Y. Guo, H.J. Feng, Q. Wang, S. Cheng, P. Cui, Z.Z. Yang, Boosting Li-O2 battery performance via coupling of P-N site-rich N, P co-doped graphene-like carbon nanosheets with nano-CePO4, Small 19 (2023) e2206455.
[35] J.J. Liu, Z.X. Wei, Z.C. Gong, M.M. Yan, Y.F. Hu, S.L. Zhao, G.L. Ye, H.L. Fei, Single-atom CoN4 sites with elongated bonding induced by phosphorus doping for efficient H2O2 electrosynthesis, Appl. Catal. B 324 (2023) 122267.
[36] Q.D. Ruan, Q. Feng, J.J. Feng, Y.J. Gao, L. Zhang, A.J. Wang, High-activity Fe3C as pH-universal electrocatalyst for boosting oxygen reduction reaction and zinc-air battery, Small (2023) e2300136.
[37] C.C. Xin, W.Z. Shang, J.W. Hu, C. Zhu, J.Y. Guo, J.W. Zhang, H.P. Dong, W. Liu, Y. T. Shi, Integration of morphology and electronic structure modulation on atomic iron-nitrogen-carbon catalysts for highly efficient oxygen reduction, Adv. Funct. Mater. 32 (2021) 2108345.

[38] M.K. Wang, T.H. Liao, X.L. Zhang, J.L. Cao, S.Q. Xu, H. Tang, Y. Wang, Electrospun carbon nanofibers loaded with atomic FeN_x /Fe_2O_3 active sites for efficient oxygen reduction reaction in both acidic and alkaline media, Adv. Mater. Interfaces 9 (2022) 2101904.

[39] T.H. Nguyen, P.K.L. Tran, D.T. Tran, T.N. Pham, N.H. Kim, J.H. Lee, Single (Ni, Fe) atoms and ultrasmall core@shell Ni@Fe nanostructures dual-implanted cnts-graphene nanonetworks for robust zn- and al-air batteries, Chem. Eng. J. 440 (2022) 135781.

[40] Y.Z. Zhou, R.H. Lu, X.F. Tao, Z.J. Qiu, G.B. Chen, J. Yang, Y. Zhao, X.L. Feng, K. Mullen, Boosting oxygen electrocatalytic activity of Fe-N-C catalysts by phosphorus incorporation, J. Am. Chem. Soc. 145 (2023) 3647–3655.

[41] J.R. Cheng, C.J. Lyu, H.R. Li, J.W. Wu, Y. Hu, B. Han, K.L. Wu, M. Hojamberdiev, D.S. Geng, Steering the oxygen reduction reaction pathways of N-carbon hollow spheres by heteroatom doping, Appl. Catal. B 327 (2023) 122470.

[42] Y. Yan, H.Y. Cheng, Z.H. Qu, R. Yu, F. Liu, Q.W. Ma, S.L. Zhao, H. Hu, Y. Cheng, C. Y. Yang, Z.F. Li, X.L. Wang, S.Y. Hao, Y.Y. Chen, M.K. Liu, Recent progress on the synthesis and oxygen reduction applications of Fe-based single-atom and double-atom catalysts, J. Mater. Chem. A 9 (2021) 19489–19507.

[43] K. Li, S.B. Zhang, X.L. Zhang, S. Liu, H.S. Jiang, T.L. Jiang, C.Y. Shen, Y. Yu, W. Chen, Atomic tuning of single-atom Fe-N-C catalysts with phosphorus for robust electrochemical CO_2 reduction, Nano Lett. 22 (2022) 1557–1565.

[44] H.S. Jiang, J. Xia, L. Jiao, X.M. Meng, P.F. Wang, C.S. Lee, W.J. Zhang, Ni single atoms anchored on N-doped carbon nanosheets as bifunctional electrocatalysts for urea-assisted rechargeable zn-air batteries, Appl. Catal. B 310 (2022) 121352.

[45] H. Xu, M. Jin, J. Geng, S.B. Zhang, H.M. Zhang, Bacterial cellulose-regulated synthesis of metallic Ni catalysts for high-efficiency electrosynthesis of hydrogen peroxide, Sci. China Mater. 65 (2021) 721–731.

[46] H.L. Meng, S.Y. Lin, J.J. Feng, L. Zhang, A.J. Wang, Coordination regulated pyrolysis synthesis of ultrafine $FeNi/(FeNi)_9S_8$ nanoclusters/nitrogen, sulfur-codoped graphitic carbon nanosheets as efficient bifunctional oxygen electrocatalysts, J. Colloid Interface Sci. 610 (2022) 573–582.

[47] H.G. Li, J.J. Wang, R.J. Qi, Y.F. Hu, J.N. Zhang, H.B. Zhao, J.J. Zhang, Y.F. Zhao, Enhanced Fe 3d delocalization and moderate spin polarization in Fe-Ni atomic pairs for bifunctional ORR and OER electrocatalysis, Appl. Catal. B 285 (2021) 119778.

[48] Q.D. Ruan, L.L. Liu, D.H. Wu, J.J. Feng, L. Zhang, A.J. Wang, Cobalt phosphide nanoparticles encapsulated in manganese, nitrogen co-doped porous carbon nanosheets with rich nanoholes for high-efficiency oxygen reduction reaction, J. Colloid Interface Sci. 627 (2022) 630–639.

[49] X.Y. Lu, H. Xu, P.X. Yang, L.H. Xiao, Y.Q. Li, J.Y. Ma, R.P. Li, L.L. Liu, A.M. Liu, V. Kondratiev, O. Levin, J.Q. Zhang, M.Z. An, Zinc-assisted MgO template synthesis of porous carbon-supported $Fe-N_x$ sites for efficient oxygen reduction reaction catalysis in zn-air batteries, Appl. Catal. B 313 (2022) 121454.

[50] D.J. Deng, J.C. Qian, X.Z. Liu, H.P. Li, D. Su, H.N. Li, H.M. Li, L. Xu, Non-covalent interaction of atomically dispersed Cu and Zn pair sites for efficient oxygen reduction reaction, Adv. Funct. Mater. 32 (2022) 2203471.

[51] L. Zhang, L.L. Liu, J.J. Feng, A.J. Wang, Methanol-induced assembly and pyrolysis preparation of three-dimensional N-doped interconnected open carbon cages supported $FeNb_2O_6$ nanoparticles for boosting oxygen reduction reaction and zn-air battery, J. Colloid Interface Sci. 661 (2024) 102–112.

[52] Z.Y. Chen, X.Z. Su, J. Ding, N. Yang, W.B. Zuo, Q.Y. He, Z.M. Wei, Q. Zhang, J. Q. Huang, Y.M. Zhai, Boosting oxygen reduction reaction with Fe and Se dual-atom sites supported by nitrogen-doped porous carbon, Appl. Catal., B 308 (2022) 121206.

[53] M. Jiang, F. Wang, F. Yang, H. He, J. Yang, W.J. Zhang, J.Y. Luo, J.J. Zhang, C. P. Fu, Rationalization on high-loading iron and cobalt dual metal single atoms and mechanistic insight into the oxygen reduction reaction, Nano Energy 93 (2022) 106793.

[54] M. Ma, A. Kumar, D.N. Wang, Y.Y. Wang, Y. Jia, Y. Zhang, G.X. Zhang, Z.F. Yan, X. M. Sun, Boosting the bifunctional oxygen electrocatalytic performance of atomically dispersed Fe site via atomic Ni neighboring, Appl. Catal. B 274 (2020) 119091.

[55] J.-E. Tsai, W.X. Hong, H. Pourzolfaghar, W.H. Wang, Y.Y. Li, A Fe-Ni-Zn triple single-atom catalyst for efficient oxygen reduction and oxygen evolution reaction in rechargeable zn-air batteries, Chem. Eng. J. 460 (2023) 141868.

[56] K. Yuan, D. Lutzenkirchen-Hecht, L.B. Li, L. Shuai, Y.Z. Li, R. Cao, M. Qiu, X. D. Zhuang, M.K.H. Leung, Y.W. Chen, U. Scherf, Boosting oxygen reduction of single iron active sites via geometric and electronic engineering: nitrogen and phosphorus dual coordination, J. Am. Chem. Soc. 142 (2020) 2404–2412.

[57] Q. Wu, L.J. Yang, X.Z. Wang, Z. Hu, Mesostructured carbon-based nanocages: an advanced platform for energy chemistry, Sci. China Chem. 63 (2020) 665–681.